Sensors & Actuators: B. Chemical 321 (2020) 128467

Contents lists available at ScienceDirect

Sensors and Actuators B: Chemical

journal homepage: www.elsevier.com/locate/snb

# The effects of size and content of cerium oxide nanoparticles on a composite sensor for hydroxyl radicals detection

Surachet Duanghathaipornsuk[a], Faisal A.O. Alateeq[a], Steve S. Kim[b], Dong-Shik Kim[a], Ana C. Alba-Rubio[a,*]

[a] Department of Chemical Engineering, The University of Toledo, Toledo, OH, USA
[b] 711th Human Performance Wing, Air Force Research Laboratory, Wright-Patterson AFB, OH, USA

ARTICLE INFO

*Keywords:*
Hydroxyl radicals
Electrochemical sensor
Cerium oxide
Cyclic voltammetry
Composite sensor

ABSTRACT

A screen-printed carbon electrode was modified with a composite comprised of cerium oxide nanoparticles and graphene oxide (CeNP/GO) to be employed as a sensing device for hydroxyl radicals (•OH) detection. $CeO_2$ nanoparticles (CeNPs) were synthesized using a precipitation method, and the CeNP/GO composites were fabricated using a low-temperature solution process. Scanning Transmission Electron Microscopy (STEM) and Energy Dispersive Spectroscopy (EDS) were used to determine the average size and the distribution of CeNPs on the composites. X-Ray powder Diffraction (XRD) confirmed the composition of the CeNP/GO composites. Cyclic voltammetry (CV) was used to characterize the interaction of the composite sensor with ˙OH generated by the Fenton reaction. The effects of size and content of CeNPs on the sensor response with ˙OH were examined using 8, 12, and 16 nm CeNPs with loadings of 10, 25, 50, 75, and 90 wt% CeNPs on the CeNP/GO composite. The CeNP/GO composite with 8 nm CeNPs showed the largest sensor response to ˙OH for all the tested ratios. Furthermore, the composites containing 50 wt% of CeNPs demonstrated the largest sensor responses in the detection of ˙OH. The lowest detection limit (0.085 mM) was observed with the composite consisting of 8 nm CeNPs with a CeNP:GO ratio of 50:50. It is thought that the lower content of GO and the aggregation of CeNPs as the loading ratio increased above 50 wt% resulted in lower current changes and poor sensor performance.

## 1. Introduction

Free radicals, which have an unpaired electron in the outer electron shell, are found both inside and outside human cells [1]. They are necessary for cells to properly maintain their functions and immune responses, such as activating the heme oxygenase [2], the transcription factor nuclear factor NF-κB [3], eliminating bacteria [4], and inactivating viruses [5]. However, a proper level of free radical production is key to maintain their advantages, as their overproduction may lead to irreversible cell damage. Among all free radicals, hydroxyl radicals (•OH) are the most reactive and dangerous ones, with a short lifetime of nanoseconds. Hydroxyl radicals can be generated inside cells, mitochondria [6], human blood [7], and interstitial fluid [8]; therefore, ˙OH have been reported to be used as biomarkers for aging, Alzheimer's or Parkinson's diseases [9]. Various detection techniques have been used to investigate the relationship between the generation of ˙OH and those diseases [10,11], and electrochemical methods have been proved to be fast, easy, practical, and inexpensive [12], although their sensitivity and selectivity to ˙OH still have room for improvement. For the electrochemical interaction with free radicals, both biological [13,14] and inorganic molecules [15,16] have been used to modify electrode surfaces for enhancing the sensitivity and selectivity towards ˙OH. However, the use of biological molecules faces the downside of denaturation [17] and instability at certain pHs and temperatures [18], causing a decreased sensor performance. To overcome these challenges, the use of some metallic materials with enzyme mimetic properties has been extensively investigated for better detection of free radicals using optical methods [19–21]. However, organic polymers or inorganic elements have rarely been used for the detection of ˙OH by electrochemical methods [22–24]. Recently, cerium oxide ($CeO_2$) has emerged as a potential scavenger for ˙OH [25–27]. Until now, cerium oxide nanoparticles (CeNPs) have been actively used for eliminating ˙OH induced by the oxidative stress for preventing cell damage [28,29]. For example, Popov et al. injected CeNPs into a culture of primary mouse fibroblasts *in vitro* and found that they reduced the level of ˙OH. Importantly, CeNPs were able to increase the survival rate of mice exposed to X-ray radiation by 60 % [30]. Another set of studies conducted by Tarnuzzer et al. showed that CeNPs protect 99 % of normal cells from

* Corresponding author.
*E-mail address:* ana.albarubio@utoledo.edu (A.C. Alba-Rubio).

https://doi.org/10.1016/j.snb.2020.128467
Received 23 March 2020; Received in revised form 9 June 2020; Accepted 13 June 2020
Available online 20 June 2020

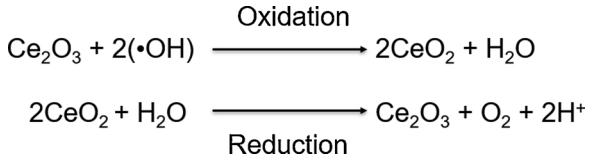


**Fig. 1.** Redox reaction scheme of CeNPs with ˙OH.

the radiation-induced free radicals that caused cell death [31].

The outstanding ability of cerium oxide for scavenging ˙OH is due to its unique dual oxidation state, which can easily switch between $Ce^{3+}$ and $Ce^{4+}$ by reducing or oxidizing species in a medium. Besides, the $Ce^{3+}$ oxidation state is considered to act as the active site for the redox reaction that scavenges ˙OH [32], as illustrated in Fig. 1 [33]. The relationship between the $CeO_2$ morphologies and the amount of $Ce^{3+}$ sites have been intensively investigated [34,35]. It was found that the particle size is one of the most important factors that determine the amount of $Ce^{3+}$ sites. Deshpande et al. observed that the $Ce^{3+}/(Ce^{3+} + Ce^{4+})$ ratio increased from 0.17 to 0.44 when reducing the $CeO_2$ particle size from 30 nm to 3 nm [36]. Zhang et al. also reported that the particle size had a remarkable impact on the amount of $Ce^{3+}$ sites on the surface. They found that the amount of $Ce^{3+}$ sites was 0.016 for 15 nm CeNPs, while it was 0.094 for 6.1 nm CeNPs. Interestingly, there were not $Ce^{3+}$ sites when the particles were larger than 5000 nm [37]. Thus, the scavenging activity of CeNPs towards ˙OH is related to the particle size due to the amount of $Ce^{3+}$ sites on the surface. Filippi et al. reported the effects of the size and shape of CeNPs on the ˙OH scavenging capacity. They observed that the scavenging capacity of 25 nm CeNPs was better than that of 50 nm CeNPs, and this difference could be explained by the larger surface area and higher defect density on smaller CeNPs [38]. Consequently, it seems crucial to determine the optimum particle size and content of CeNPs for constructing a highly sensitive and selective electrochemical composite sensor for ˙OH detection.

In the present study, a carbon electrode was modified with a composite consisting of CeNPs and graphene oxide (GO). The size of the CeNPs and the ratio between CeNPs and GO were varied to investigate their relationship with the sensing performance of the composites towards ˙OH. As previously mentioned, the scavenging capacity of CeNPs was reported to be greatly affected by their particle size; therefore, it has been hypothesized that the size and content of CeNPs would be important design parameters for optimizing the sensor performance. To overcome the poor conductivity of CeNPs, graphene oxide (GO) was chosen as the second component of the sensor composite. GO was selected due to its high intrinsic conductivity and surface area [39]. The effect of the CeNPs size on the reactivity with ˙OH was examined using 8, 12, and 16 nm CeNPs. For the effect of the loading ratio, 10, 25, 50, 75, and 90 wt% of CeNPs were used in the CeNP/GO composite.

## 2. Experimental section

### 2.1. Materials and characterization methods

Cerium(III) nitrate hexahydrate (> 99 %), graphene oxide, potassium hexacyanoferrate(II) trihydrate (98.5–102.0 %), potassium hexacyanoferrate(III) (> 99 %), iron(III) chloride (97 %), iron(II) sulfate heptahydrate (≥99 %), potassium chloride (≥99 %), and 30 wt% hydrogen peroxide solution were obtained from Sigma-Aldrich (USA). Screen-printed carbon electrodes (Pine Instruments, USA) coated with a 2 mm carbon working electrode, Ag/AgCl reference electrode, and carbon counter electrode were used as the sensor base. The sizes of the as-synthesized CeNPs and CeNPs on the composites were determined by using a scanning transmission electron microscope, STEM Hitachi HD-2300A (Japan). The compositions of the CeNP/GO composites were confirmed by using a Rigaku Ultima III X-ray Diffractometer with Small Angle X-ray Scattering (SAXS). XRD patterns were obtained using the 2θ range from 20° to 90° operating with a Cu target and Cu Kα radiation of 0.15406 nm wavelength at a power rating of 40 kV and 44 mA. The crystallite size was determined by the Scherrer equation. Cyclic voltammetry (CV) measurements were performed using a Gamry Reference 600 potentiostat (Gamry Instruments, USA).

### 2.2. Synthesis of cerium oxide nanoparticles (CeNPs)

Cerium oxide nanoparticles (CeNPs) were synthesized by the precipitation method described by Chen et al. [40]. Briefly, 50 mL of a cerium nitrate solution was mixed with 25 mL of a 3 M $NH_4OH$ solution. The operating temperatures were varied depending on the desired CeNPs size, being these 30, 80, and 120 °C for 8, 12, and 16 nm particle sizes, respectively. After 2 h, the resulting product was recovered and rinsed with deionized water several times. Then, the CeNPs were dried in an oven at 60 °C for 12 h. After that, the CeNPs were stored at room temperature in a desiccator. XRD and STEM were then used to determine the average CeNPs particle size.

### 2.3. Synthesis of CeNP/GO composites

For the synthesis of the CeNP/GO composites, 100 mg of CeNPs and GO with different weight ratios were mixed in 100 mL of deionized water. For example, 10 mg of CeNPs and 90 mg of GO were used for the preparation of the 10:90 ratio CeNP/GO composite. The dispersion of CeNPs and GO in deionized water was then placed in an ultra-sonication bath for 1 h to homogenize the mixed solution. Following sonication, the dispersion was stirred for 2 h to obtain the CeNP/GO composite. The solid sample was collected by centrifugation and dried at 60 °C for 12 h. Once dried, the solid was grounded to a fine powder and kept in a desiccator at room temperature. XRD and STEM/EDS were used to confirm the presence of CeNPs and GO in the composite matrix.

### 2.4. Deposition of the CeNP/GO composite on a screen-printed carbon electrode

10 mg of CeNP/GO composite was suspended in 10 mL of deionized water. The solution was then sonicated for 1 h and deposited onto the working electrode by delivering a single drop (8 µL) using a micropipette. The droplet was dried in an oven at 60 °C for 1 h. Once dried, the sensor was rinsed with deionized water and dried by gently flowing nitrogen gas. Cyclic voltammetry (CV) was used to confirm the presence of the composite on the electrode surface. The potential range selected for CV was from -0.8 V to 0.8 V with a scan rate of 100 mV/s using a 5 mM solution of $[Fe(CN)_6]^{3-/4-}$ in a mixture of 0.1 M KCl and phosphate-buffered saline (PBS) buffer solution at pH 7.2.

### 2.5. Detection of ˙OH by the CeNP/GO-modified electrode

The Fenton reaction was used to generate ˙OH for CV experiments. By mixing equal volumes of 10 mM solutions of $H_2O_2$ and $FeSO_4{\cdot}7H_2O$, the Fenton reaction produces ˙OH via the reduction of $H_2O_2$ in the presence of $Fe^{2+}$ ions. The composite-modified electrode was then inserted into the Fenton reaction to detect ˙OH by using CV. The first cycle of CV was carried out using the $H_2O_2$ solution. After that, the electrode was removed from the solution, and then an equal volume of the 10 mM iron(II) sulfate solution was added to generate ˙OH. Then, the electrode was immersed in the solution again to detect the presence of ˙OH. The potential range selected for CV was from 0.4 V to −0.6 V with 100 mV/s of scan rate. Both the reduction and oxidation responses (i.e., redox response) in the cyclic voltammogram were used to calculate the redox response ($\Delta A$) of the sensor due to the redox reaction between the composite and ˙OH. The redox response was calculated using the procedure described in Fig. 2, in which $\Delta A$ is taken from the difference between the currents at the oxidation and reduction peaks.

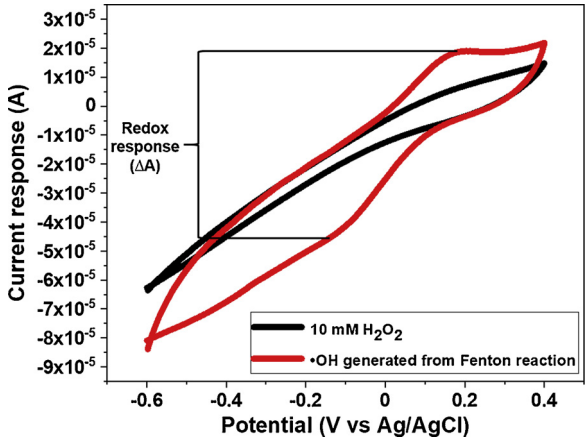


**Fig. 2.** Calculation of the redox response ($\Delta A$) of 10 mM $H_2O_2$ and ˙OH generated from the Fenton reaction (10 mM $H_2O_2$ + 10 mM $FeSO_4{\cdot}7H_2O$).

The CV curve for $H_2O_2$ showed no significant redox peaks, which proved that there was no considerable redox reaction between the CeNP/GO-modified electrode and $H_2O_2$.

## 3. Results and discussion

### 3.1. Synthesis of CeNPs and CeNP/GO composites

CeNPs were synthesized by precipitation at various temperatures to obtain different particle sizes. STEM was used to characterize the particle size, shape, and aggregation of CeNPs. Fig. S1 (Supporting Information) shows STEM images of the CeNPs synthesized at different temperatures: 30, 120, and 150 °C, and they show their typical cubic and hexagonal structures. XRD experiments were performed to determine the average particle sizes of CeNPs. As shown in Fig. S2, diffractograms (a–c), which correspond to CeNPs with different particle sizes, exhibit identical diffraction peaks at 28.4° (111), 32.9° (200), 47.3° (220), 56.1° (311), 58.8° (222), 69.3° (400), 76.5° (331), and 78.9° (420), which comply with the standard cubic structure of $CeO_2$ (JCPDS 65–2975) [41,42]. Fig. S2, diffractograms (d–f) show the same eight diffraction peaks for the CeNP/GO composites, which means that the composites were successfully synthesized by the low-temperature solution process at room temperature. Another important evidence that validates the success of the synthesis protocol is the disappearance of the light yellowish color of the CeNPs dispersion after contacting with GO.

The effect of the synthesis temperature on the particle size of CeNPs was investigated by XRD. As demonstrated in Fig. S2, diffractograms (a–c), when increasing the synthesis temperature, the intensity of $CeO_2$ peaks increases, which confirms the influence of the different synthesis temperatures on the CeNPs particle size. The Scherrer equation, based on the eight diffraction peaks, was used to determine the average particle size of CeNPs. Average diameters of 8, 12, and 16 nm were obtained for the CeNPs synthesized at 30, 120, and 150 °C, respectively. Thus, this confirms that the $CeO_2$ particle size can be controlled by the temperature of the hydrothermal method. XRD experiments also confirmed the presence of CeNPs on the composites.

As stated before, a suitable amount of CeNPs is required on the composite for the optimum design of the sensor electrode. STEM images were also used to investigate the effect of CeNP loading on the GO surface. Fig. 3 shows the different STEM images obtained with the 8 nm CeNP/GO composite with different CeNP:GO weight ratios, 10:90, 25:75, 50:50, 75:25, and 90:10. As expected, the presence of CeNPs on the composite increases when increasing the amount of CeNPs added at the beginning of the synthesis of CeNP/GO composites. The EDS maps in Fig. 3b, d, f, h, j verify that the composites consist of CeNPs and GO, as both Ce (white) and C (blue) elements are presented throughout the samples. As the content of CeNPs increases, white dots become more dominant. It is readily noticeable that the largest aggregation of CeNPs happened in those composites with high CeNP/GO ratios, which reduced both the contact area and the amount of $Ce^{3+}$ sites available for ˙OH scavenging. For example, when comparing the composites with CeNP:GO ratios of 25:75 (Fig. 3c) and 75:25 (Fig. 3g), it is observed that the degree of aggregation in 75:25 is important, being difficult to identify individual CeNPs. Similar TEM images representing the aggregation of CeNPs have been reported in the literature [43,44]. In contrast, the 8 nm CeNP/GO composite with a CeNP:GO weight ratio of 50:50 (Fig. 3e) shows a homogenous dispersion of the CeNPs on the GO surface. High dispersion of CeNPs on the composite is thought to result in higher availability of $Ce^{3+}$ sites to conduct the redox reaction with ˙OH, which can improve the efficiency of the composite sensor for the detection of ˙OH.

### 3.2. Effects of the CeNPs size and loading on the sensor conductivity

In order to determine the influence of the $CeO_2$ nanoparticles size and loading ratio on the sensor performance for the detection of ˙OH, CV was conducted with various CeNP/GO composites. Fig. 4 shows all cyclic voltammograms obtained with 8, 12, and 16 nm CeNP/GO composites with different CeNP:GO weight ratios, which were employed in a 5 mM solution of $[Fe(CN)_6]^{3-/4-}$ in a mixture of 0.1 M KCl and phosphate-buffered saline (PBS) buffer solution at pH 7.2 (no generation of ˙OH). As can be seen in Fig. 4a–c, the current response increases when the CeNP:GO weight ratio decreases, and the same trend is observed with 8, 12, and 16 nm CeNP/GO composites. For example, the current response of 8 nm CeNP/GO increases 2 and 4 times when decreasing the CeNP:GO weight ratio from 90:10 to 50:50 and 10:90, respectively. This could be explained in terms of the increased amount of highly conductive material (GO) and the decrease of the poorly conductive element (CeNPs) on the composite. Therefore, the results in Fig. 4a–c confirm the influence of the loading ratio on the sensor conductivity, which has a great impact on the sensor efficiency for ˙OH detection.

Remarkably, the particle size of CeNPs also influences the sensor conductivity (Fig. 4d). When comparing the different particle sizes using a CeNP:GO weight ratio of 50:50, the largest conductivity was obtained with the composite containing 8 nm CeNPs. This could be explained by the higher dispersion of the small CeNPs on the GO surface, which contributes to a shorter distance for electron transfer between the electrode surface and the electrolyte solution in comparison to large size nanoparticles. With a shorter path for electron transfer, the composites with small CeNPs have higher conductivities, as shown in the comparison of 8, 12, and 16 nm for CeNP:GO (50:50 ratio) (Fig. 4d). It can be then concluded that both the CeNPs size and its content on the composite have a significant effect on the conductivity of the sensor.

### 3.3. Effects of the CeNPs size on the detection of hydroxyl radicals

As reported by Filippi et al., [38] there is a direct correlation between the particle size and the amount of $Ce^{3+}$ sites that control the ˙OH scavenging capacity of CeNPs. The density of $Ce^{3+}$ sites per mass of CeNPs increases as the particle size decreases, which results in more redox reaction between CeNPs and ˙OH. Furthermore, a composite with small particle size possesses a larger surface area per unit mass for contacting and reacting with ˙OH. Here we hypothesized that the size of the CeNPs might have a significant impact on the sensor performance for the detection of ˙OH. Fig. S3 shows the cyclic voltammograms obtained with the 50:50 CeNP/GO composite sensor containing CeNPs of different sizes in the presence of ˙OH. While there is no redox reaction in the presence of $H_2O_2$ solution, there are redox peaks in the presence of ˙OH. The redox curves are the result of the reaction between $Ce^{3+}$ sites and ˙OH, as described in Fig. 1. These results confirm the ability of

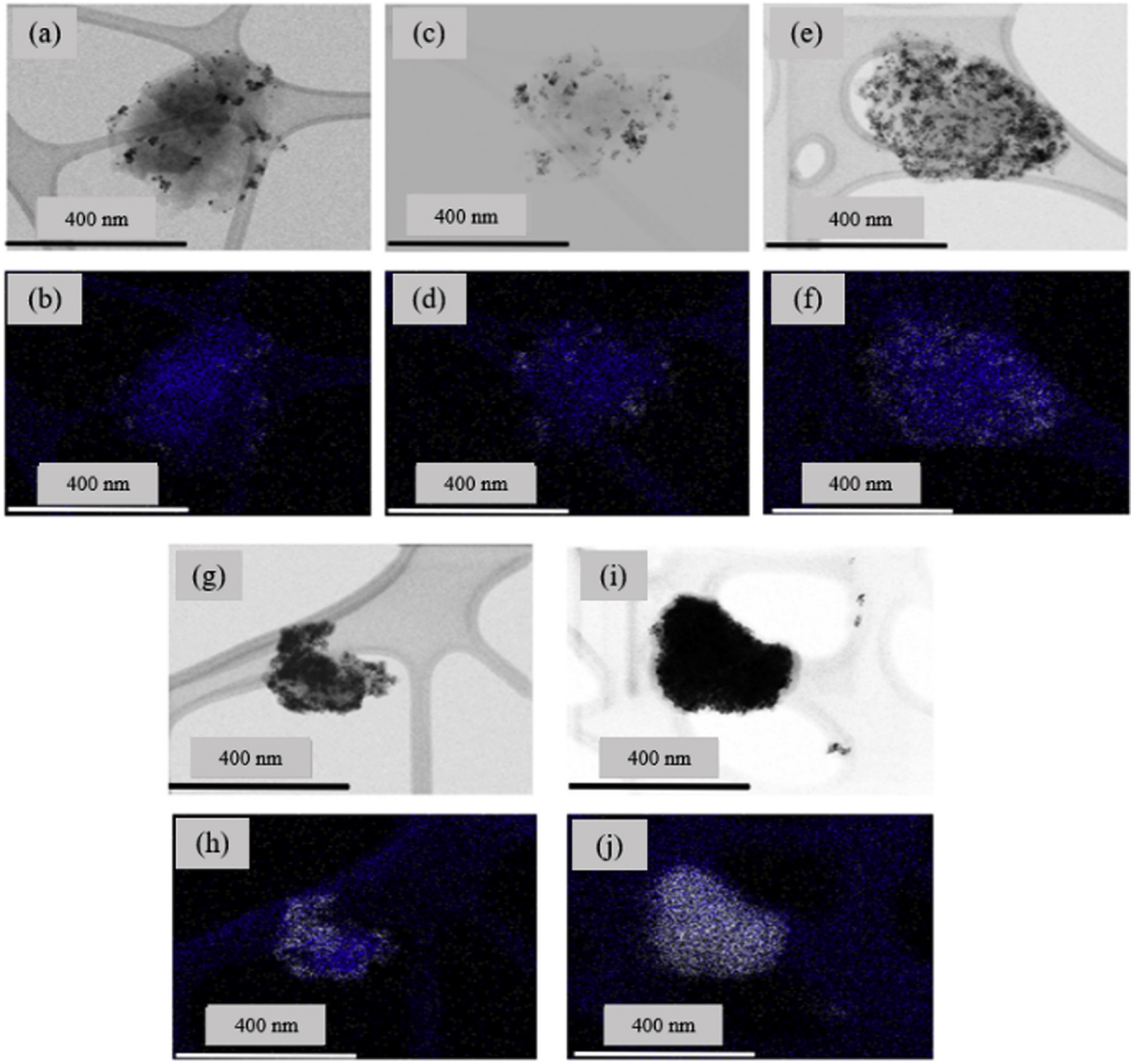


**Fig. 3.** STEM images and EDS maps of 8 nm CeNP/GO composites with CeNP:GO ratios of (a, b) 10:90, (c, d) 25:75, (e, f) 50:50, (g, h) 75:25, and (i, j) 90:10.

the CeNP/GO composite-modified electrode to react with ˙OH, whereas it shows no distinguishable redox peaks with $H_2O_2$.

Fig. 5 clearly shows that 8 nm CeNPs provide the largest $\Delta A$ due to the redox reaction regardless of the CeNP:GO ratio used. The redox response increases as the size of CeNPs decreases for all the loading ratios tested except for CeNP:GO = 90:10. The effect of the loading ratio on $\Delta A$ is further explained in Section 3.4. Our experimental results, thus, verify our hypothesis that the CeNPs size has a great impact on the sensor performance for ˙OH detection. This is because the smaller the CeNPs are, the larger surface area and the greater amount of $Ce^{3+}$ sites per unit mass they have, which are the active sites for the reaction with ˙OH.

### 3.4. Effects of the CeNPs loading on the detection of hydroxyl radicals

As previously stated, the sensor response for the detection of ˙OH depends not only on the CeNPs size but also on its loading ratio on the CeNP/GO composite. Consequently, different CeNP:GO weight ratios were examined to find the relationship between them. CeNP:GO weight ratios of 10:90, 25:75, 50:50, 75:25 and 90:10 were used to synthesize the composites. Fig. 5 demonstrates that the loading of CeNPs in the composite greatly affected the sensor response to ˙OH. The redox response increases with the addition of CeNPs until reaching a maximum at CeNP:GO ratio of 50:50, and it decreases with ratios higher than that. A similar performance was obtained with all the composite sensors with different CeNPs sizes. It is noted that the trend observed in Fig. 5 differs from that in Fig. 4. This is due to the fact that the CeNP/GO composite-modified electrode in Fig. 5 was tested in the Fenton reaction for the detection of ˙OH. As mentioned earlier, CeNPs were used as the sensing element, and GO was used to improve the conductivity of the composite. On the other hand, in Fig. 4, the CeNP/GO composite-modified electrode was tested in the electrolyte solution of $[Fe(CN)_6]^{3-/4-}$ without generating ˙OH. Thus, the content of GO is the main factor controlling the sensor response in the electrolyte solution.

The results in Fig. 5 confirm that the CeNPs size and loading ratio play important roles in the detection of ˙OH. As stated before, even though CeNPs contain redox-active sites, i.e., $Ce^{3+}$, its low conductivity makes them a poor choice as a sensing element. However, the integration with GO successfully provided a high dispersion of the nanoparticles and increased overall conductivity, as shown in Figs. 3 and 4. Even when $\Delta A$ increases with the addition of CeNPs until reaching a maximum at CeNP:GO = 50:50 ratio for all different CeNPs sizes (Fig. 5), it is worth to highlight that the best sensor response was obtained with the smaller particle size (8 nm). When the CeNP:GO ratio increases from 25:75 to 50:50 ratio, the 8 nm CeNP/GO composite shows 1.8 times increase in $\Delta A$ as compared to 1.3 and 1.2 times for 12 and 16 nm, respectively. It is assumed that this is because of the high amount of $Ce^{3+}$ sites when using CeNPs of smaller size. However, 12

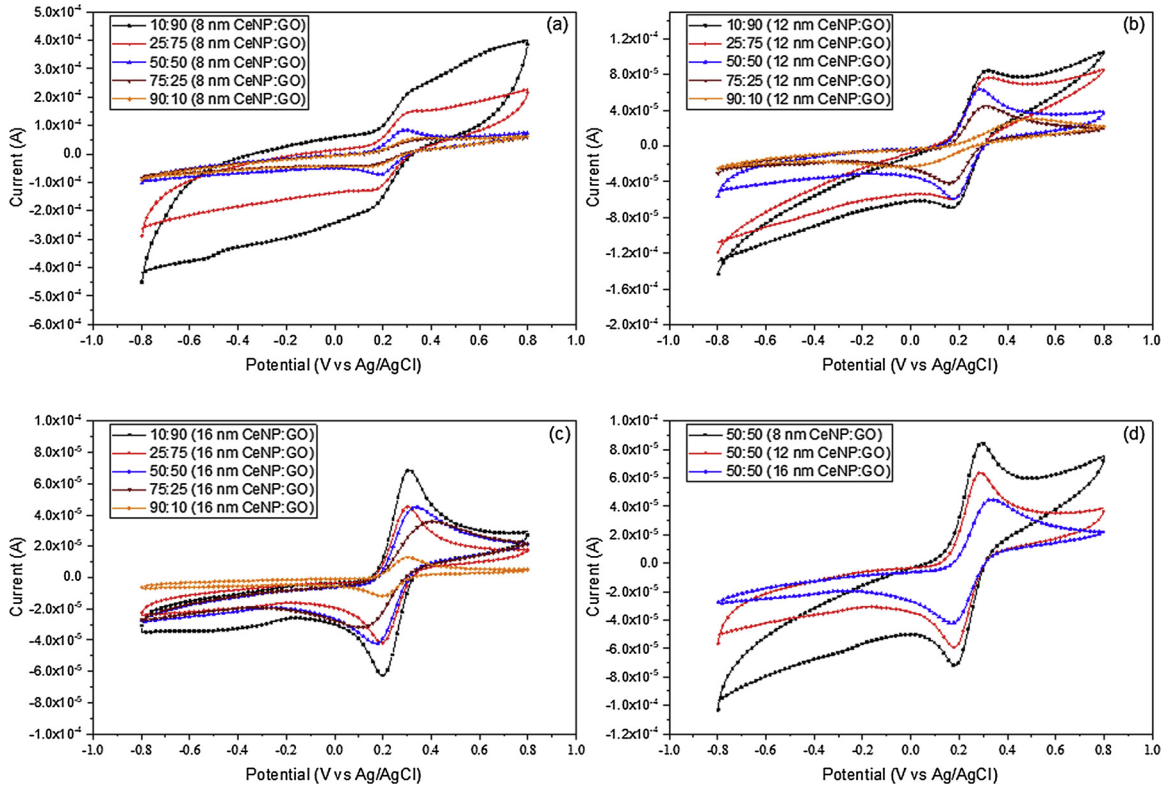


**Fig. 4.** CV results of the CeNP/GO composites with different CeNPs sizes and loading ratios: (a) 8 nm, (b) 12 nm, and (c) 16 nm CeNP/GO composites; and (d) comparison of CV results with 8, 12 and 16 nm CeNP/GO composites with a 50:50 CeNP:GO weight ratio. Evaluation of the sensor conductivity: no ˙OH were generated for these experiments.

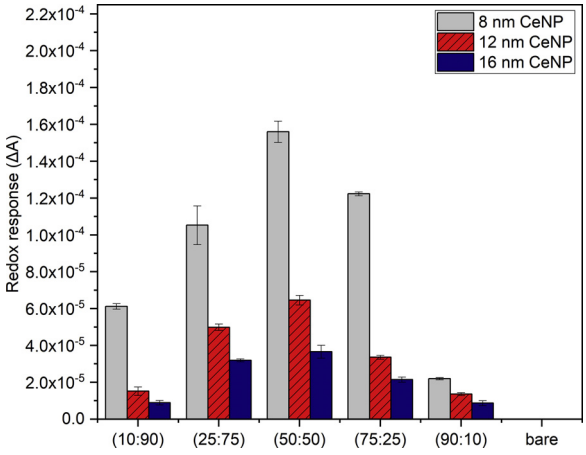


**Fig. 5.** Relationship between the redox response ($\Delta A$) and the size and content of the CeNPs on the composite. The error bars represent the standard deviation of 3 repetitive measurements.

and 16 nm CeNPs do not show an equivalent degree of increased sensor response. This could be due to the small number of $Ce^{3+}$ sites for ˙OH scavenging when using 12 and 16 nm CeNPs. Even when increasing the CeNPs loading from 25:75 to 50:50 CeNP:GO weight ratio, there is no significant increase in the amount of $Ce^{3+}$ sites, which might also be due to the aggregation of CeNPs.

The CeNP/GO composites with lower CeNP:GO ratios (10:90 and 25:75) also provided smaller $\Delta A$ compared to the 50:50 composite ratio, even though the conductivity of the composites was high due to the high content of GO. This is likely due to the low loading of CeNPs and the lack of $Ce^{3+}$ sites for ˙OH detection when using 10:90 and 25:75 ratios. Lower $\Delta A$ were also observed for CeNP:GO ratios above 50:50 (i.e., 75:25 and 90:10), which might be attributed to a lower conductivity resulting from a lesser content of GO. For the loading ratios of 10:90, 25:75, 50:50, and 75:25, $\Delta A$ of the 8 nm CeNP/GO composite is 4.0, 2.4, 2.5, and 3.7 times greater than 12 nm, and 7.0, 3.3, 4.3, and 5.7 times greater than 16 nm composites, respectively. However, $\Delta A$ of the 8 nm CeNP/GO composite at 90:10 ratio shows a dramatic decrease from that of 75:25, and it is only 1.5 and 2.0 times greater than those of 12 and 16 nm CeNPs. Therefore, there might be other factors influencing the decrease of $\Delta A$ at high ratios. It is thought that the aggregation of 8 nm CeNPs at high loading results in the reduction of both the overall surface area and the amount of $Ce^{3+}$ sites available for ˙OH detection. By having both a lower surface area and amount of $Ce^{3+}$ sites, $\Delta A$ of the 8 nm CeNP/GO composite with 90:10 ratio is considerably smaller, and only slightly higher than those with 12 and 16 nm CeNP/GO composites. Furthermore, the electron transfer between the active sites and the electrode surface could be retarded by the aggregation of CeNPs. The largest $\Delta A$ was obtained with the 8 nm CeNP/GO composite with CeNP:GO = 50:50 wt ratio. With equal masses of CeNPs and GO, CeNPs are thought to be homogeneously dispersed onto the surface of GO with less aggregation, which results in a great amount and exposure of $Ce^{3+}$ sites for reacting with ˙OH. In summary, the size of CeNPs and the ratio of CeNPs and GO in the composite were successfully controlled to optimize the sensor response towards ˙OH.

### 3.5. Composite sensitivity toward hydroxyl radicals

Three 50:50 CeNP/GO composites sensors with different CeNPs sizes of 8, 12, and 16 nm were used to determine the limit of detection (LOD) for ˙OH detection. The concentration of ˙OH generated from the Fenton reaction was varied between 0.1 and 10 mM. Regardless of the size of the CeNPs in the composite, the composite sensor shows a linear relationship between $\Delta A$ and the concentration of ˙OH, as shown in

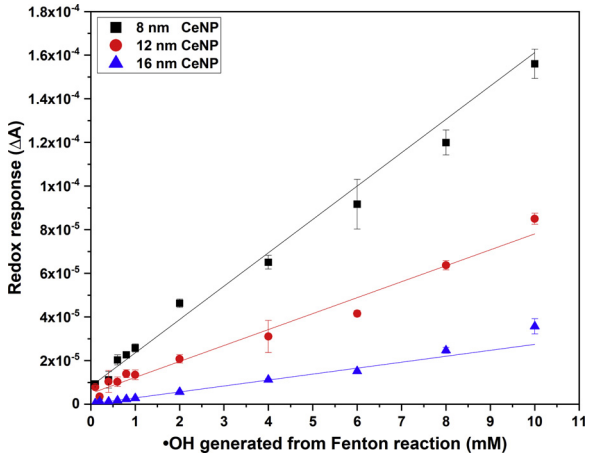


**Fig. 6.** Limits of detection of the CeNP/GO composites with different CeNPs sizes. ˙OH were generated from the Fenton reaction (10 mM $H_2O_2$ + 10 mM $FeSO_4{\cdot}7H_2O$). The error bars represent the standard deviation of 3 repetitive measurements.

Fig. 6. It also shows that the CeNPs size has a significant impact on $\Delta A$ to different ˙OH concentrations. The 8 nm CeNP/GO composite shows the largest $\Delta A$ when compared to those with 12 and 16 nm CeNPs for all the tested ˙OH concentrations. The equation (3.3 × SD)/b was used to determine the limit of detection (LOD) [45], where SD represents the standard deviation of the blank, and b is the slope of the regression line. The detection limit was found to be lowered when smaller CeNPs were used as 8, 12, 16 nm CeNPs resulted in LODs of 0.085, 0.18, and 0.47 mM, respectively. Again, these results confirm the impact of the CeNPs size on the sensor efficiency towards the detection of ˙OH.

## 4. Conclusions

A CeNP-based GO composite electrochemical sensor was investigated for the detection of hydroxyl free radicals. The particle size and content of CeNPs in the composite appeared to control the sensor response towards ˙OH. An electrode modified with the 8 nm CeNP/GO composite with the CeNP:GO weight ratio of 50:50 showed the largest sensor response towards ˙OH with the lowest detection limit of 0.085 mM of •OH. The smaller the size of CeNPs was, the greater the sensor response from the redox reaction for all the tested loading ratios. The 50:50 loading ratio between CeNPs and GO showed the largest response for all the studied CeNPs sizes. The sensor response decreased when the content of CeNPs was higher than 50 wt% because of the low conductivity of the composite as a result of the low content of GO. The dramatic decrease of the sensor response for the 8 nm CeNP/GO composite with the 90:10 ratio is attributed to the aggregation of CeNPs at a high loading of CeNPs. To the best of our knowledge, this is the first time that a CeNP/GO composite is used as an effective sensing element for ˙OH detection through an electrochemical mechanism. This composite could be used for developing real-time mediatorless sensors for medical diagnosis. Furthermore, it could be used for environmental, cosmetics, and food sample analyses, and any other related areas in which ˙OH need to be monitored or controlled.

## CRediT authorship contribution statement

**Surachet Duanghathaipornsuk:** Methodology, Validation, Formal analysis, Investigation, Data curation, Writing - original draft, Visualization. **Faisal A.O. Alateeq:** Investigation. **Steve S. Kim:** Resources, Supervision, Project administration, Funding acquisition. **Dong-Shik Kim:** Conceptualization, Methodology, Formal analysis, Investigation, Resources, Data curation, Writing - review & editing, Visualization, Supervision, Project administration, Funding acquisition. **Ana C. Alba-Rubio:** Methodology, Formal analysis, Resources, Writing - review & editing, Supervision, Project administration, Funding acquisition.

## Declaration of Competing Interest

The authors declare no competing financial interest.

## Acknowledgements

This material is based upon work supported by the National Science Foundation under Grant No. 1817294. D.S.K. acknowledges support from the Air Force Summer Faculty Fellowship Program (SFFP) for his research stay at the 711th Human Performance Wing, Air Force Research Lab, to conduct research on this project.

## Appendix A. Supplementary data

Supplementary material related to this article can be found, in the online version, at https://doi.org/10.1016/j.snb.2020.128467.

## References

[1] I.S. Young, J.V. Woodside, Antioxidants in health and disease, J. Clin. Pathol. 54 (2001) 176–186.
[2] S.M. Keyse, R.M. Tyrrell, Heme oxygenase is the major 32-kDa stress protein induced in human skin fibroblasts by UVA radiation, hydrogen peroxide, and sodium arsenite, Proc. Natl. Acad. Sci. 86 (1989) 99–103.
[3] R. Schreck, P.A. Baeuerle, A role for oxygen radicals as second messengers, Trends Cell Biol. 1 (1991) 39–42.
[4] M.R. Green, H.A.O. Hill, M.J. Okolow-Zubkowska, A.W. Segal, The production of hydroxyl and superoxide radicals by stimulated human neutrophils-measurements by EPR spectroscopy, FEBS Lett. 100 (1979) 23–26.
[5] E. Bachere, E. Mialhe, D. Noel, V. Boulo, A. Morvan, J. Rodriguez, Knowledge and research prospects in marine mollusc and crustacean immunology, Aquaculture 132 (1995) 17–32.
[6] J. Vásquez-Vivar, B. Kalyanaraman, M.C. Kennedy, Mitochondrial aconitase is a source of hydroxyl radical an electron spin resonance investigation, J. Biol. Chem. 275 (2000) 14064–14069.
[7] B. Lipinski, Hydroxyl radical and its scavengers in health and disease, Oxid. Med. Cell. Longev. 2011 (2011) 1–9.
[8] A.V. Crowe, A. McArdle, F. McArdle, D.M. Pattwell, G.M. Bell, G.J. Kemp, J.M. Bone, R.D. Griffiths, M.J. Jackson, Markers of oxidative stress in the skeletal muscle of patients on haemodialysis, Nephrol. Dial. Transplant. 22 (2007) 1177–1183.
[9] B.J. Tabner, S. Turnbull, O.M. El-Agnaf, D. Allsop, Formation of hydrogen peroxide and hydroxyl radicals from Aβ and α-synuclein as a possible mechanism of cell death in Alzheimer's disease and Parkinson's disease, Free Radic. Biol. Med. 32 (2002) 1076–1083.
[10] T. Obata, Role of hydroxyl radical formation in neurotoxicity as revealed by in vivo free radical trapping, Toxicol. Lett. 132 (2002) 83–93.
[11] P. Teismann, B. Ferger, The salicylate hydroxylation assay to measure hydroxyl free radicals induced by local application of glutamate in vivo or induced by the Fenton reaction in vitro, Brain Res. Protoc. 5 (2000) 204–210.
[12] A. Khoshroo, L. Hosseinzadeh, A. Sobhani-Nasab, M. Rahimi-Nasrabadi, H. Ehrlich, Development of electrochemical sensor for sensitive determination of oxazepam based on silver-platinum core–shell nanoparticles supported on graphene, J. Electroanal. Chem. Lausanne (Lausanne) 823 (2018) 61–66.
[13] S. Ding, M. Li, H. Gong, Q. Zhu, G. Shi, A. Zhu, Sensitive and selective measurement of hydroxyl radicals at subcellular level with tungsten nanoelectrodes, Anal. Chem. 92 (2020) 2543–2549.
[14] A. Hájková, J. Barek, V. Vyskočil, Electrochemical DNA biosensor for detection of DNA damage induced by hydroxyl radicals, Bioelectrochemistry 116 (2017) 1–9.
[15] I. Gualandi, L. Guadagnini, S. Zappoli, D. Tonelli, A polypyrrole based sensor for the electrochemical detection of OH radicals, Electroanal 26 (2014) 1544–1550.
[16] C. Iffelsberger, T. Raith, P. Vatsyayan, V. Vyskočil, F.-M. Matysik, Detection and imaging of reactive oxygen species associated with the electrochemical oxygen evolution by hydrodynamic scanning electrochemical microscopy, Electrochim. Acta 281 (2018) 494–501.
[17] X. Liu, X. Liu, H. Wei, G. Song, H. Guo, X. Lu, Sensitive detection of superoxide anion released from living cells using silver nanoparticles and functionalized multiwalled carbon nanotube composite, Sens. Actuators B Chem. 252 (2017) 503–510.
[18] H. Zhang, X. Cai, H. Zhao, W. Sun, Z. Wang, M. Lan, Enzyme-free electrochemical sensor based on ZIF-67 for the detection of superoxide anion radical released from SK-BR-3 cells, J. Electroanal. Chem. 855 (2019) 1–8.
[19] J.M. George, A. Antony, B. Mathew, Metal oxide nanoparticles in electrochemical sensing and biosensing: a review, Microchim. Acta 185 (2018) 1–26.
[20] M.-Q. Wang, C. Ye, S.-J. Bao, M.-W. Xu, Controlled synthesis of $Mn_3(PO_4)_2$ hollow

spheres as biomimetic enzymes for selective detection of superoxide anions released by living cells, Microchim. Acta 184 (2017) 1177–1184.
[21] F. Peng, T. Xu, F. Wu, C. Ma, Y. Liu, J. Li, B. Zhao, C. Mao, Novel biomimetic enzyme for sensitive detection of superoxide anions, Talanta 174 (2017) 82–91.
[22] Z. Wang, K. Yi, Q. Lin, L. Yang, X. Chen, H. Chen, Y. Liu, D. Wei, Free radical sensors based on inner-cutting graphene field-effect transistors, Nat. Commun. 10 (2019) 1–10.
[23] J.-Y. Fang, C.-H. Chu, I. Sarang, K.-C. Fang, C.-P. Hsu, Y.-F. Huang, C.-H. Hsu, C.-C. Chen, S.-S. Li, J.A. Yeh, Electronic hydroxyl radical microsensors based on the conductivity change of polyaniline, Sens. Actuators B Chem. 208 (2015) 99–105.
[24] Y. Xu, D. Wang, Y. Zhang, J. Zhang, S. Jiang, W. Liang, T. Zhu, B.-C. Ye, A novel electrochemical sensor for determination of hydroxyl radicals in living cells by coupling nanoporous gold layer with self-assembled 6-(Ferrocenyl) hexanethiol, Anal. Chim. Acta 1096 (2020) 69–75.
[25] Y. Xue, Q. Luan, D. Yang, X. Yao, K. Zhou, Direct evidence for hydroxyl radical scavenging activity of cerium oxide nanoparticles, J. Phys. Chem. C 115 (2011) 4433–4438.
[26] S. Zou, X. Zhu, L. Zhang, F. Guo, M. Zhang, Y. Tan, A. Gong, Z. Fang, H. Ju, C. Wu, Biomineralization-inspired synthesis of cerium-doped carbonaceous nanoparticles for highly hydroxyl radical scavenging activity, Nanoscale Res. Lett. 13 (2018) 1–10.
[27] H. Wu, L. Shabala, S. Shabala, J.P. Giraldo, Hydroxyl radical scavenging by cerium oxide nanoparticles improves Arabidopsis salinity tolerance by enhancing leaf mesophyll potassium retention, Environ. Sci. Nano 5 (2018) 1567–1583.
[28] M. Das, S. Patil, N. Bhargava, J.-F. Kang, L.M. Riedel, S. Seal, J.J. Hickman, Auto-catalytic ceria nanoparticles offer neuroprotection to adult rat spinal cord neurons, Biomaterials 28 (2007) 1918–1925.
[29] Y. Li, X. He, J.-J. Yin, Y. Ma, P. Zhang, J. Li, Y. Ding, J. Zhang, Y. Zhao, Z. Chai, Z. Zhang, Acquired superoxide-scavenging ability of ceria nanoparticles, Angew. Chem. Int. Ed. 54 (2015) 1832–1835.
[30] A. Popov, S. Zaichkina, N. Popova, O. Rozanova, S. Romanchenko, O. Ivanova, A. Smirnov, E. Mironova, I. Selezneva, V. Ivanov, Radioprotective effects of ultra-small citrate-stabilized cerium oxide nanoparticles in vitro and in vivo, RSC Adv. 6 (2016) 106141–106149.
[31] R.W. Tarnuzzer, J. Colon, S. Patil, S. Seal, Vacancy engineered ceria nanostructures for protection from radiation-induced cellular damage, Nano Lett. 5 (2005) 2573–2577.
[32] P. Trogadas, J. Parrondo, V. Ramani, $CeO_2$ surface oxygen vacancy concentration governs in situ free radical scavenging efficacy in polymer electrolytes, ACS Appl. Mater. Interfaces 4 (2012) 5098–5102.
[33] J.M. Perez, A. Asati, S. Nath, C. Kaittanis, Synthesis of biocompatible dextran-coated nanoceria with pH-dependent antioxidant properties, Small 4 (2008) 552–556.
[34] J.E. Spanier, R.D. Robinson, F. Zhang, S.-W. Chan, I.P. Herman, Size-dependent properties of $CeO_{2-y}$ nanoparticles as studied by Raman scattering, Phys. Rev. B 64 (2001) 1–8.
[35] S. Schlick, M. Danilczuk, A.R. Drews, R.S. Kukreja, Scavenging of hydroxyl radicals by Ceria nanoparticles: effect of particle size and concentration, J. Phys. Chem. C 120 (2016) 6885–6890.
[36] S. Deshpande, S. Patil, S.V.N.T. Kuchibhatla, S. Seal, Size dependency variation in lattice parameter and valency states in nanocrystalline cerium oxide, Appl. Phys. Lett. 87 (2005) 1–3.
[37] F. Zhang, P. Wang, J. Koberstein, S. Khalid, S.-W. Chan, Cerium oxidation state in ceria nanoparticles studied with X-ray photoelectron spectroscopy and absorption near edge spectroscopy, Surf. Sci. 563 (2004) 74–82.
[38] A. Filippi, F. Liu, J. Wilson, S. Lelieveld, K. Korschelt, T. Wang, Y. Wang, T. Reich, U. Pöschl, W. Tremel, H. Tong, Antioxidant activity of cerium dioxide nanoparticles and nanorods in scavenging hydroxyl radicals, RSC Adv. 9 (2019) 11077–11081.
[39] N. Akkarachanchainon, P. Rattanawaleedirojn, O. Chailapakul, N. Rodthongkum, Hydrophilic graphene surface prepared by electrochemically reduced micellar graphene oxide as a platform for electrochemical sensor, Talanta 165 (2017) 692–701.
[40] H.-I. Chen, H.-Y. Chang, Synthesis of nanocrystalline cerium oxide particles by the precipitation method, Ceram. Int. 31 (2005) 795–802.
[41] S. Kumar, A.K. Ojha, D. Patrice, B.S. Yadav, A. Materny, One-step in situ synthesis of CeO2 nanoparticles grown on reduced graphene oxide as an excellent fluorescent and photocatalyst material under sunlight irradiation, Phys. Chem. Chem. Phys. 18 (2016) 11157–11167.
[42] S. Wang, F. Gao, Y. Zhao, N. Liu, T. Tan, X. Wang, Two-dimensional $CeO_2$/RGO composite-modified separator for lithium/sulfur batteries, Nanoscale Res. Lett. 13 (2018) 1–9.
[43] J.F. Berret, A. Sehgal, M. Morvan, O. Sandre, A. Vacher, M. Airiau, Stable oxide nanoparticle clusters obtained by complexation, J. Colloid Interface Sci. 303 (2006) 315–318.
[44] M.-S. Tsai, The study of the synthesis of nano-grade cerium oxide powder, Mater. Lett. 58 (2004) 2270–2274.
[45] A. Shrivastava, V. Gupta, Methods for the determination of limit of detection and limit of quantitation of the analytical methods, Chron. Young Sci. 2 (2011) 21–25.

**Surachet "Ray" Duanghathaipornsuk** is a chemical engineering Ph.D. candidate co-advised by Drs. Alba-Rubio and Kim. Ray has played a critical role in developing innovative sensors for reactive oxygen species (ROS), including hydroxyl free radicals and hydrogen peroxide, as well as developing an α-prototype of the sensor for the detection of hydroxyl radicals. Ray has co-invented a free radical sensor (US 2019/0212286 A1) and a super-sensitive free radical sensor (provisional patent filed). Ray has presented his free radical sensors at multiple local and national conferences, including the ECS meeting in Dallas, TX in 2019, and the ACS National Meeting in Boston, MA in 2018. Ray was the recipient of the UToledo College of Engineering Outstanding Translational Research Award in 2019.

**Faisal Abdulaziz O. Alateeq** is a quality engineer in Middle East Battery Company (MEBCO) for manufacturing of automotive maintenance free lead-acid batteries (AC Delco brand) in Dammam Second Industrial City, Saudi Arabia. He received an associate degree in Chemical Engineering Technology from Jubail Industrial College, Saudi Arabia, in 2013. He then enrolled as a quality technician in Ma'aden Aluminum Company for cooperative education (co-op). Then, he moved to USA, where he earned a B.S. degree in Chemical Engineering from the University of Toledo in December 2018. During his undergraduate studies, he conducted another co-op rotation as an environmental specialist in Royal Commission, Jubail Industrial City, Saudi Arabia, in 2017. He worked as a research assistant in Dr. Kim's lab during his last co-op in 2018. His research focused on synthesizing cerium oxide nanoparticles/graphene oxide composites as a sensing element for detecting hydroxyl radicals.

**Dr. Steve Kim** serves as a Research Physical Scientist within the Applied Biotechnology Branch at the 711th Human Performance Wing, Air Force Research Laboratory (AFRL) Wright-Patterson AFB, OH. Dr. Kim obtained his Ph.D. degree in Polymer Science from the University of Connecticut (2007). After completing National Research Council Postdoctoral Fellow (2007–2010), Dr. Kim continued to work as a contract research scientist at AFRL (2010–2016). Dr. Kim's research interest is in developing electronic/electrochemical/optical molecular biomarker and chemical sensors. Dr. Kim leads research on developing an electronic biosensor platform for trace level cognitive molecular biomarkers, a crucial piece of information to increase the human performance monitoring/assessment capability for the United States Air Force (USAF). Dr. Kim has authored and coauthored 48 peer-reviewed scientific journal articles.

**Dr. Dong-Shik Kim** is a professor of chemical engineering at the University of Toledo since 2000. Dr. Kim received B.S. and M.S. degrees from Seoul National University, Korea, and a Ph.D. degree from the University of Michigan, USA, all in chemical engineering. At the University of Toledo, Dr. Kim has worked on various research projects including enzymes, anti-fouling agents, polysaccharides, and bio-/nano-sensors. He has published 60 articles in peer-reviewed journals with 1800 citations (h-index 27). He has six US and international patents. Dr. Kim is a registered professional engineer in Michigan. He was a recipient of a Fulbright Distinguished Chair Award in 2018.

**Dr. Ana C. Alba-Rubio** is an Assistant Professor in the Department of Chemical Engineering at the University of Toledo, OH (USA). She received a B.S. in Chemical Engineering from the University of Málaga, Spain, in 2007. She then moved to the Institute of Catalysis and Petrochemistry (CSIC) in Madrid, Spain, to pursue her doctoral studies. As a doctoral student, she enjoyed two short research stays in Brazil and the Netherlands. After receiving her Ph.D., Dr. Alba-Rubio joined the Department of Chemical and Biological Engineering at the University of Wisconsin-Madison to conduct post-doctoral research. In 2015, she joined the University of Toledo as a faculty, and her current research interests involve the rational design and synthesis of nanomaterials for catalysis and sensing applications. She has co-authored more than 20 publications in peer-reviewed journals with more than 1400 citations (h-index 18), 1 book chapter, and multiple contributions to national and international conferences. She is also a co-inventor in four patent applications.